Critical current density and vortex phase diagram in the superconductor $Sn_{0.55}In_{0.45}Te$

Yiming Wang,[1,*] Mingtao Li,[1,*] Cuiying Pei,[2] Lingling Gao,[2] Kejun Bu,[1] Dong Wang,[1] Xuqiang Liu,[1,3] Limin Yan,[1,4] Jia Qu,[1,4] Nana Li,[1] Bihan Wang,[1] Yifei Fang,[5] Yanpeng Qi,[2,6,7,†] and Wenge Yang[1,‡]

[1]*Center for High Pressure Science and Technology Advanced Research, Shanghai 201203, China*
[2]*School of Physical Science and Technology, ShanghaiTech University, Shanghai 201210, China*
[3]*Key Laboratory for Anisotropy and Texture of Materials, Northeastern University, Shenyang 110819, China*
[4]*State Key Laboratory of Superhard Materials and Department of Physics, Jilin University, Changchun 130012, China*
[5]*State Key Laboratory of High Field Laser Physics, Shanghai Institute of Optics and Fine Mechanics (SIOM), Chinese Academy of Sciences (CAS), Shanghai 201800, China*
[6]*ShanghaiTech Laboratory for Topological Physics, ShanghaiTech University, Shanghai 201210, China*
[7]*Shanghai Key Laboratory of High-resolution Electron Microscopy, ShanghaiTech University, Shanghai 201210, China*

(Received 11 January 2022; revised 21 July 2022; accepted 22 July 2022; published 5 August 2022)

Critical current density and vortex pinning dynamics have been studied in the superconductor $Sn_{0.55}In_{0.45}Te$. Analysis of the temperature-dependent lower critical field shows that it has a weakly anisotropic single energy gap. The critical current density $J_c(0)$ and pinning potential $U_0(H)$ values reach as high as 2.56×10^3 A/cm^2 at 1.8 K and 2.1×10^3 K at $\mu_0 H = 0.01$ T, respectively. Based on the collective pinning model, we demonstrate the coexistence of vortex pinning regimes in $Sn_{0.55}In_{0.45}Te$. One is a δT_c pinning regime induced by the spatial fluctuations of the transition temperature in a low field. The other is a dominantly δl pinning regime associated with the spatial variations of the charge-carrier mean free path in a higher field. This causes a nonconstant exponent of the power-law behavior $J_c(T) \propto H^n$. A very weak vortex fluctuation is unveiled by a narrow separation between the irreversibility field $\mu_0 H_{irr}(T)$ and upper critical field $\mu_0 H_{c2}(T)$ in the vortex phase diagram. We discuss the potential application in superconducting electronics like the single-photon detector in thin film form.

DOI: 10.1103/PhysRevB.106.054506

I. INTRODUCTION

SnTe has been widely studied as a prototype topological crystalline insulator with a narrow direct band gap of 0.18–0.31 eV [1–3]. By alloying [4] and strain-engineering [5], it achieves great thermoelectric performance. Through Indium doping [6,7], enhanced superconductivity appears with a tunable superconducting transition temperature (T_c) by adjusting the In content, ranging from 24 mK to 5.1 K [6–8]. At the lower In-doping side for $x < 0.12$ [9], the observation of a zero-bias conductance peak in $Sn_{1-x}In_xTe$ ($x = 0.045$) with preserved topological surface state indicates that it hosts topological superconductivity [10,11]. Nevertheless, the nuclear magnetic resonance (NMR) experiment shows that the polycrystalline $Sn_{0.96}In_{0.04}Te$ is a spin-singlet superconductor [12]. When x exceeds 0.12 [9], one theoretical work points out that the $Sn_{1-x}In_xTe$ becomes a Dirac semimetal, or a Weyl semimetal through a ferroelectric effect or Jahn-Teller distortion although lacking of further experimental verifications. The combined possible topological nontrivial band structure and superconductivity in $Sn_{1-x}In_xTe$ makes it a fertile platform for exploring a variety of fermions and new topological states of matter [9,11].

Despite intensive studies that have been reported on the bulk $Sn_{1-x}In_xTe$ superconductors, we need to note that the nature of its superconducting state is still under debate. The London penetration depth measurements on $x = 0.10$ and 0.45 [13], muon-spin spectroscopy measurements on $x = 0.38 - 0.45$ [14], and thermal conductivity measurements on $x = 0.40$ [15] have evidenced the fully gapped superconducting state, which can be described by the s-wave Bardeen-Cooper-Schrieffer (BCS) theory [13,14]. These results lead to the controversy on its topological superconductivity nature for $Sn_{1-x}In_xTe$ superconductors. Furthermore, based on superconducting density functional theory (SCDFT) and tunneling spectroscopy, Nomoto *et al.* revealed that the spin-orbit coupling (SOC) can largely enhance T_c at a low carrier region and the T_c of $Sn_{1-x}In_xTe$ can be quantitatively described by the conventional s-wave BCS scenario [16]. In addition, the disorder induced by the increase of Sn content in InTe or In content in SnTe can broaden the features of the density of states (DOS) spectral function [7,16], which leads to the redistribution of spectral weight and the mild changes of DOS at Fermi level $N(E_F)$ with the dopant amount. It is also shown that the evolution of $N(E_F)$ positively correlates the T_c vs. x in $Sn_{1-x}In_xTe$ superconductors [7].

Recently, to explore the junctions or devices applications, thin films of $Sn_{1-x}In_xTe$ with various In-doping contents have

*Y.W. and M.T.L. contributed equally to this work.
†qiyp@shanghaitech.edu.cn
‡yangwg@hpstar.ac.cn

been successfully grown on substrates by molecular beam epitaxy and pulsed-laser deposition [17–20]. $Sn_{1-x}In_xTe$ thin films grown on a Bi_2Te_3 buffer layer show a coexistence of bulk and topological surface superconductivity [18]. Masuko *et al.* reported superconducting $Sn_{1-x}In_xTe$ thin films with $x = 0.66$ [20], beyond the bulk solubility limit of $x = 0.5$. These studies pave the way for their possible device applications. For instance, a combination of the tunable T_c, large normal state resistivity, with the higher slope of upper critical field vs. temperature in superconducting thin films makes them being candidate materials for single-photon detector (SNSPD) application [21,22]. Also, the avoided large $N(E_F)$ due to In doping also benefits for developing a SNSPD using $Sn_{1-x}In_xTe$ candidates [7,16]. However, the critical current density and vortex pinning dynamics in $Sn_{1-x}In_xTe$ remain unexplored, which are important ingredients for applications [23]. Moreover, there is a discrepancy on the energy gap ratio determined by London penetration depth and muon-spin spectroscopy for the $x = 0.45$ composition [13,14], which needs a further investigation using an alternative technique.

Here, we choose $Sn_{0.55}In_{0.45}Te$, the optimal doping level with maximum T_c for the ambient pressure growth, to investigate the critical current density and vortex dynamics in its Dirac semimetal superconductor form [6,7]. Through the magnetic and electrical transport measurements, we established the vortex pinning phase diagram and derived a few key physical parameters, which are important for superconducting electronics applications.

II. EXPERIMENTAL METHODS

A. Sample synthesis and characterizations

The experimental SnTe and $Sn_{0.55}In_{0.45}Te$ bulk single crystals were synthesized via the melt method in a vertical furnace. The Sn (6N, Alfa Aesar), In (4N, Alfa Aesar), and Te (6N, Alfa Aesar) granules with a stoichiometric ratio were put into an evacuated quartz tube with a conical bottom and then sealed by the hydrogen-oxygen flame. The mixtures were heated at 1123 K for 12 h followed by cooling to 1018 K at a rate 1.5 K/h and annealing at 1018 K for more than 24 h, and the SnTe and $Sn_{0.55}In_{0.45}Te$ ingots were obtained by quenching into an ice water bath. Specially rectangle-shaped single crystals of SnTe were found on the top part of the ingot.

A piece of rectangle-shaped specimen (size: $2.75\times2.66\times0.80$ mm^3) was used for the magnetic and electrical transport measurements. Electrical transport measurements were performed using the standard four-probe method on a DynaCool physical property measurement system (PPMS). Isothermal magnetization hysteresis loops (MHLs) and initial magnetization measurements were conducted on a superconducting quantum interference device vibrating sample magnetometer. The temperature range was between 1.8 and 5.1 K with an interval of $\Delta T = 0.3$ K. The ramping rate for collecting MHLs was 20 Oe/s and 1.6 Oe/s for the initial magnetization.

The phase purity was confirmed by the laboratory PANalytical Empyrean x-ray diffraction (XRD) system with a Cu Kα1 radiation source. Single crystal XRD measurements were performed on a Bruker D8 VENTURE diffractometer with Ag target ($\lambda = 0.561$ Å) and Mo target ($\lambda = 0.717$ Å) for SnTe and In-doped samples. The single crystal XRD data were refined by ARPEX3 software and the structural parameters can be found in Supplemental Material [24]. The Rietveld refinement of the powder XRD patterns was further processed using the GSAS program package with the user interface EXPGUI [25,26]. The compositions were determined by energy-dispersive x-ray spectroscopy (EDS) and the inductively coupled plasma atomic emission spectroscopy (ICP-AES).

B. Theoretical calculations

All calculations were done in the framework of DFT [27,28] using the projector augmented wave [29,30] pseudopotential method, as implemented in the VASP package [31,32]. The electron exchange-correlation functional was treated in generalized gradient approximation as proposed by Perdew-Burke-Ernzerhof. The valance electrons were considered as $4d^{10}5s^25p^2$ for Sn, $4d^{10}5s^25p^1$ for In and $5s^25p^4$ for Te. The kinetic energy cutoff for the plane-wave basis set expansion was set to 360 eV in all cases to avoid Pullay stress. A Γ-centered Monkhorst-Pack grid of $7\times7\times7$ and $10\times10\times10$ k points were used for the geometry optimization and calculation of DOS, respectively. The energy convergence of 1.0×10^{-8} eV was used for the electronic energy minimization steps. During relaxation, Feynman forces on each atom were minimized until they were less than 0.001 eV/Å. SOC was taken into account in all calculations.

III. RESULTS AND DISCUSSIONS

A. Electronic band structures

Band structure calculations were performed to characterize the topological properties of SnTe and $Sn_{0.55}In_{0.45}Te$. For the bulk $Sn_{1-x}In_xTe$ systems, we used a $2\times2\times2$ supercell at the face-centered-cubic primitive cell basis, containing eight cations (Sn/In) and eight anions (Te), as illustrated in Figs. 1(a) and 1(b). Considering the complexity of calculations and the similar electronic structure of $x = 0.45$ and 0.5 doping [9], we used the structure of Sn and In evenly distributed in a 1:1 ratio. In Figs. 1(d) and 1(e) we plotted the electronic band structure and projected DOS by considering SOC effect. The high symmetry k path in the Brillouin zone for both structures is shown in Fig. 1(c). The bulk band structure of SnTe shows a gap of less than 0.2 eV at the Fermi energy level (E_F), with the band inversion occurring at the Γ point, a good ingredient for a nontrivial topological surface state [2,9]. A previous report of band inversion at the L point does not contradict our results as the L point is folded onto the Γ point with supercells consideration [33]. After alloying In atoms, the E_F is significantly lowered and $N(E_F)$ increases, leading to a metallic state for $Sn_{0.55}In_{0.45}Te$. Moreover, band inversion can still be observed at the Γ point but at a higher level near 0.9 eV. The p electrons of Sn, s electrons of In, and p electrons of Te hybridize around E_F, giving a large $N(E_F)$ that may lead to an increase in the T_c. Actually, previous reports show that the doped of In in SnTe will lead to the increase of $N(E_F)$ with adding more In atoms for $x \leqslant 0.5$, which correlates with the evolution of T_c with In content and

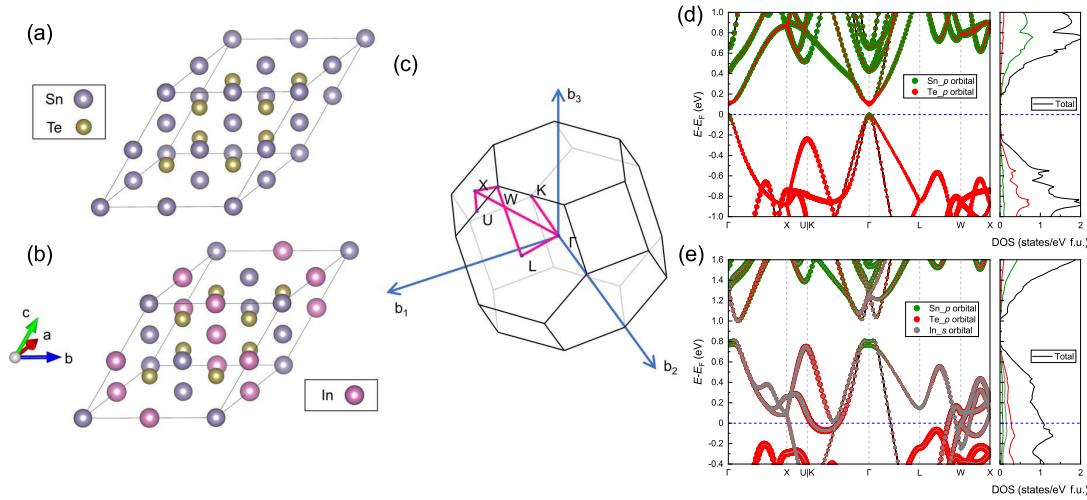

FIG. 1. Supercell structures at the face-centered cubic primitive cell basis for (a) SnTe and (b) $Sn_{0.5}In_{0.5}Te$. (c) High symmetry k path in the Brillouin zone. Band structures include SOC and projected DOS for (d) SnTe and (e) $Sn_{0.5}In_{0.5}Te$. The Fermi energy (blue dashed lines) is set to zero.

may account for the enhancement of T_c in In-doped SnTe materials [7,34].

B. Structure, composition, and superconducting properties

The cubic symmetry and phase purity are confirmed by powder XRD patterns, as shown in Fig. 2(a). Note that the weak reflection at $\sim 2\theta$ angle 33 degree is likely from the tetragonal InTe phase [6]. The Rietveld refinement yields the lattice parameter $a = 6.3092(1)$ and $a = 6.2507(2)$ for SnTe and $Sn_{0.55}In_{0.45}Te$, respectively. Representative EDS profiles are plotted in Fig. 2(b). Comparing to the pristine sample, the appearance of the excitation peaks clearly indicates the alloying In atoms in the $Sn_{1-x}In_xTe$ ($x = 0.45$) sample. To accurately analyze the composition, we have used ICP-AES technique, which gives $Sn_{0.98}Te$ and $Sn_{0.54}In_{0.45}Te$. Hereafter, we will use the nominal composition for discussions and comparison. The temperature-dependent resistivity and magnetic susceptibility at low temperature were measured to detect the superconductivity for $Sn_{0.55}In_{0.45}Te$, as shown in Fig. 2(c). The sharp diamagnetic transition below 5.10 K and the high shielding volume of 94% at 1.8 K indicate a homogeneous bulk superconductivity. This is further corroborated by the sharp zero-resistivity transition at 5.04 K shown in Fig. 2(d).

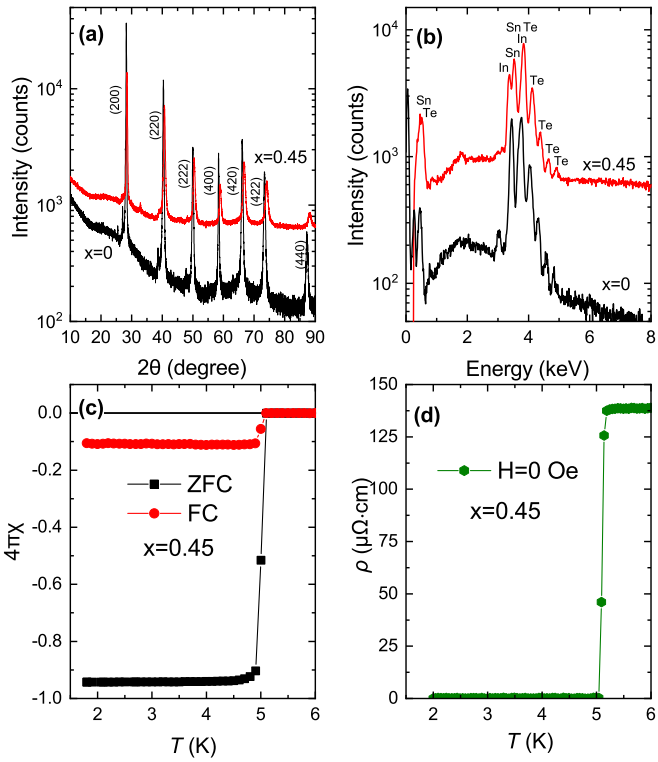

FIG. 2. (a) XRD patterns. (b) EDS spectrum. (c) and (d) show the temperature-dependent magnetic susceptibility and resistivity for $Sn_{0.55}In_{0.45}Te$.

C. Lower critical field

Initial magnetization versus applied field $M(H)$ curves was measured to verify the temperature-dependent lower critical field $\mu_0 H_{c1}$ that determines the superfluid density, as displayed in Figs. 3(a) and 3(b). The demagnetization effect was taken into account. The lower critical field $\mu_0 H_{c1}$ can be obtained by [35]

$$\mu_0 H_{c1}(T) = \frac{\mu_0 H_{p1}(T)}{1 + N \cdot \chi_{int}}, \tag{1}$$

where $\mu_0 H_{p1}(T)$ is the first penetration field. N is the demagnetization factor as is calculated by $N = [1 + (3/4)\cdot(c/a)(1 + (a/b))]^{-1}$ [35], where a, b, c are dimensions for a cuboid. Here, N is calculated to be 0.69 for our sample. The first $\mu_0 H_{p1}(T)$ is determined by the deviation from the linear behavior of the initial $M(H)$, as indicated in Fig. 3(b) and its inset for the plots of $\Delta M = M_{exp} - M_{fit}$ versus field. Here, the $M_{fit} = s \cdot \mu_0 H$ with s being the slope of the initial magnetization. The $\mu_0 H_{c1}(T)$ data follows on an empirical

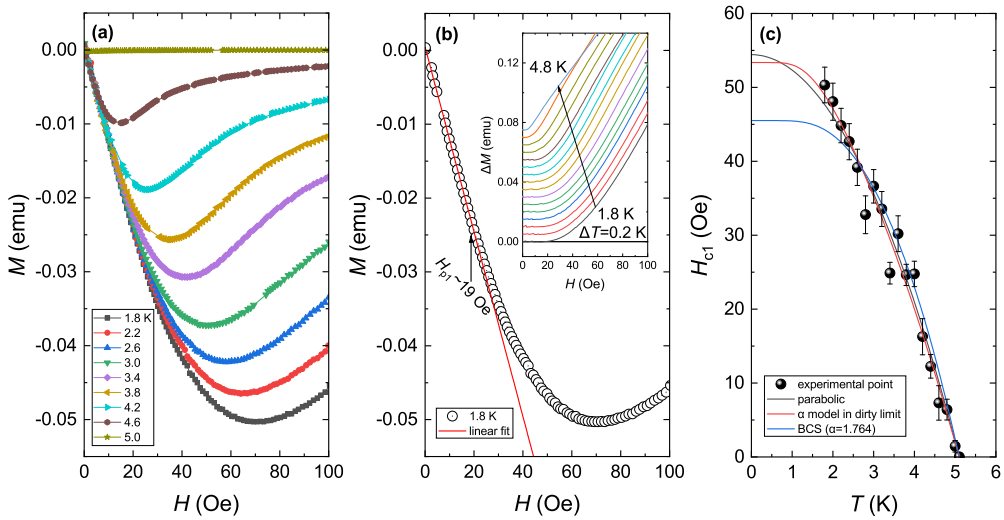

FIG. 3. (a) Initial magnetization curves vs. applied field of $Sn_{0.55}In_{0.45}Te$ at various temperatures. (b) Initial diamagnetization at 1.8 K. Solid line presents a linear fitting curve. Inset shows the difference between experimental and linear fitting data. (c) Temperature-dependent $\mu_0 H_{c1}$. Solid lines are theoretical fitting curves.

parabolic line [36]

$$\mu_0 H_{c1}(T) = \mu_0 H_{c1}(0)\left[1 - \left(\frac{T}{T_c}\right)^2\right]. \tag{2}$$

Moreover, as shown later, our sample satisfies the local limit since $\xi(0)$ is much smaller than London penetration depth $\lambda(0)$. In the local London model, the temperature-dependent superfluid density [37,38]

$$n_s(T) = \frac{\lambda^{-2}(T)}{\lambda^{-2}(0)} = \frac{\mu_0 H_{c1}(T)}{\mu_0 H_{c1}(0)}, \tag{3}$$

can be analyzed using the $\mu_0 H_{c1}(T)$. Given the metallic behavior and assuming a spherical Fermi surface, the mean free path can be estimated by $l = \hbar k_F/\rho_0 n e^2$ with the Fermi wave number $k_F = (3\pi^2 n)^{1/3}$ and residual resistivity ρ_0, yielding $l = 127(3)$ nm and 0.6(2) nm for SnTe and $Sn_{0.55}In_{0.45}Te$ [24]. The l value is much smaller than its superconducting coherence length at the 0 K limit $\xi(0) = 13.8(1)$ nm, indicating the dirty limit in $Sn_{0.55}In_{0.45}Te$. The significant decrease of product $k_F l$ that quantifies the disorder in $Sn_{0.55}In_{0.45}Te$ compared with SnTe implies the prominent disorders scattering due to the introduction of Indium atoms. In the dirty limit [37,39], the $n_s(T)$ is given by

$$n_s(T) = \frac{\Delta(T)}{\Delta_0}\tanh\left(\frac{\Delta(T)}{2k_B T}\right). \tag{4}$$

The gap function can be approximately expressed as [40]

$$\Delta(T) = \Delta_0 \tanh\left(1.82\left[1.018\left(\frac{T_c}{T} - 1\right)\right]^{0.51}\right), \tag{5}$$

where Δ_0 is the energy gap at zero temperature. According to the α model [41], the quantity $\alpha \equiv \Delta_0/k_B T_c$ can be treated as an adjustable parameter. We obtained $\alpha = 1.18 \pm 0.12$ from the best fitting, smaller than the standard BCS value $\alpha_{BCS} = 1.764$ in a weak coupling limit [42]. Both fitting results are shown in Fig. 3(c). The obtained ratio is in good agreement with the London penetration depth measurements ($\alpha = 1.18$ for $Sn_{0.55}In_{0.45}Te$) [13], but smaller than the value from muon-spin rotation or relaxation (μSR) measurements [$\alpha = 1.89(3)$ for $Sn_{0.55}In_{0.45}Te$ in clean limit] [14]. In Ref. [14], Saghir *et al.* have analyzed their $\lambda^{-2}(T)$ data using the BCS s-wave model in both clean and dirty limit. Also, they show that the Δ_0 magnitudes in the clean limit are larger than those of dirty limit, indicating a smaller gap ratio in dirty limit as demonstrated for $x = 0.45$ herein. In addition, one would expect a variable gap ratio if further considering the gap anisotropy during analyzing the $\lambda^{-2}(T)$ data by μSR measurements. Nevertheless, this calls for further studies. Furthermore, the results by thermal conductivity probes indicate that the $Sn_{0.6}In_{0.4}Te$ has a full superconducting gap [15]. Consequently, the small gap ratio of the $Sn_{0.55}In_{0.45}Te$ sample can be attributed to its weakly anisotropic single gap [13,42].

D. Critical current density and vortex pinning mechanism

The critical current density $J_c(H)$ is the maximum unimpeded current that a superconductor can transmit per unit cross section at a given temperature and magnetic field, one of the key parameters to evaluate their superconducting applications. The extended Bean critical state model was adopted to estimate the $J_c(H)$ of $Sn_{0.55}In_{0.45}Te$ [43]. Figure 4(a) shows the MHLs between 1.8 and 5.1 K with a temperature interval of $\Delta T = 0.3$ K. For a rectangle-shaped sample with field parallel to the shortest edge, the field-dependent J_c is given by

$$J_c(H) = \frac{20\Delta M}{w\left(1 - \frac{w}{3l}\right)}, \tag{6}$$

where w and l are the width and length of the sample, and ΔM is the difference between the magnetization values for the increasing and decreasing field, the sample's thickness t is set as $t < w < l$ and the magnetization is in the unit of emu/cm^3. The $J_c(0)$ at $T = 1.8$ K is extracted to be $J_c(0) = 2.56\times10^3$ A/cm^2, comparable to those iron-based high-temperature superconductors FeS [44], FeSe [45], and

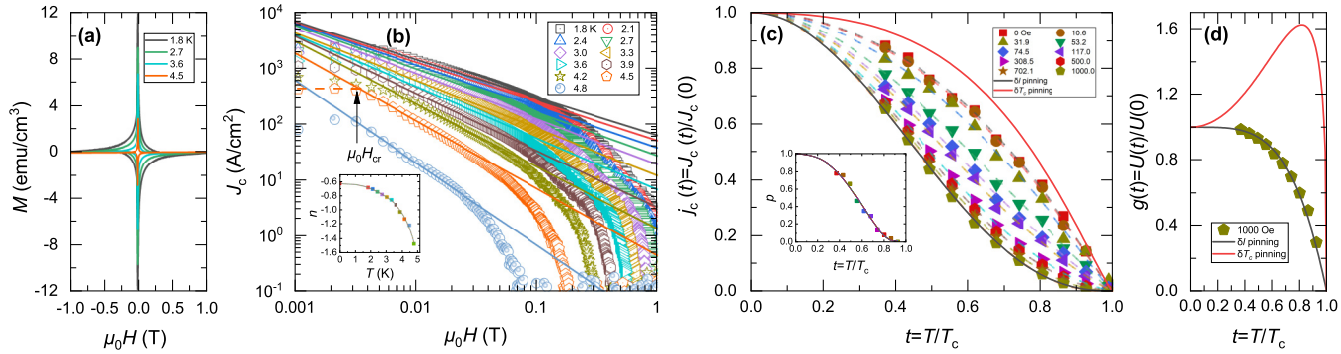

FIG. 4. (a) Magnetic hysteresis loops below 5.1 K of $Sn_{0.55}In_{0.45}Te$. (b) Log-log plot of critical current density J_c versus applied field. The J_c is extracted by Bean's model. The inset shows the exponent versus temperature. (c) Normalized $j_c(t)$. The inset shows the percentage of the pinning regime. (d) The normalized pinning energy $g(t) = U(t)/U(0)$ versus temperature.

Mn-doped $K_xFe_{2-y}Se_2$ [46]. Above a crossover field H_{cr} at 32 Oe, as indicated in Fig. 4(b), the $J_c(H)$ curves follow a power-law behavior $J_c \propto H^n$, indicative of a collective pinning signature [47–49]. However, the $J_c(H)$ deviates from the power-law scaling in a high field. The power-law behavior implies a fairly dense distribution of weak pins exists in $Sn_{0.55}In_{0.45}Te$ [50], analogous to that in $Cu_{0.10}Bi_2Se_3$ [49]. According to the strong pinning theory [23], the $J_c(H)$ is nearly constant for $H < H_{cr}$ while $J_c(H) \propto H^{-5/8}$ for $H > H_{cr}$, where H_{cr} is a crossover field in the $J_c(H)$ curve. At 1.8 K, the fitting exponent is $n = -0.682(2)$. In principle, this could approach the theoretical $n = -0.625$ by further decreasing temperature, as shown in the inset of Fig. 4(b). However, the n value has an apparent temperature dependence and tends to decline at higher temperature. This is unexpected in the strong pinning theory, which predicts a temperature-independent exponent [23].

To understand this puzzling behavior in $J_c(H)$, we conducted a pinning regime analysis for $Sn_{0.55}In_{0.45}Te$. Given it belongs to a large-κ superconductor with Ginzburg-Landau (GL) parameter $\kappa = 25(1)$, this leads us to safely assume that its core interaction plays a major role in the vortex pinning dynamics [49]. Two categories of vortex pinning, δl pinning and δT_c pinning, were considered. Based on the collective pinning theory [51], the temperature-dependent normalized $J_c(T)$ in a single-vortex pinning regime can be described by $J_c^{\delta l}(t)/J_c^{\delta l}(0) = (1-t^2)^{5/2}(1+t^2)^{-1/2}$ for δl pinning, and $J_c^{\delta T_c}(t)/J_c^{\delta T_c}(0) = (1-t^2)^{7/6}(1+t^2)^{5/6}$ for δT_c pinning with $t = T/T_c$. In addition, the functions $g(t) = U(t)/U(0)$ characterizing the temperature-dependent pinning energy are given by $g^{\delta l}(t) = 1 - t^4$ for δl pinning, and $g^{\delta T_c}(t) = (1-t^2)^{1/3}(1+t^2)^{5/3}$ for δT_c pinning. Also, taking the mixed regimes into account, we used a combined relation, $J_c(t) \propto (1-p)J_c^{\delta l}(t) + pJ_c^{\delta T_c}(t)$, to fit the experimental $J_c(T)$ data, where p is the contribution percentage by δT_c pinning. Finally, we plot the $J_c(t)$ and $g(t)$ data at different magnetic fields in Fig. 4(c). Intriguingly, the pinning is governed by the δT_c pinning in a low field and gradually transformed to a δl dominant pinning in a higher field. The inset of Fig. 4(c) shows the evolution of the contribution of δT_c pinning with simultaneously increasing temperature and field. Under 1000 Oe, the vortex pinning is governed by δl pinning, and the normalized pinning energy $g(t)$ follows the δl pinning regime well, as shown in Fig. 4(d). This result supports that the peculiar nonconstant exponent above H_{cr} arises from the synergetic interplay of the δT_c pinning and δl pinning in $Sn_{0.55}In_{0.45}Te$. Benefiting from the close-by δT_c pinning, the $Sn_{0.55}In_{0.45}Te$ material may find high J_c applications at a low temperature and small field.

From the $J_c(H)$ data, the irreversibility critical field $\mu_0 H_{irr}$ can be determined as the point at extrapolated zero J_c value from Kramer plot [52], $J_c^{1/2}H^{1/4}$ as a function of H. Figure 5 shows the Kramer plot and the linear extrapolation of solid lines lead to the $\mu_0 H_{irr}$ at $J_c = 0$. Inset of Fig. 5 presents the temperature dependent $\mu_0 H_{irr}(T)$, which can be fitted by the $\mu_0 H_{irr}(T) = \mu_0 H_{irr}(0)(1 - T/T_c)^n$. The best fitting yields $n = 1.24(3)$, comparable to that of Mn-doped $K_xFe_{2-y}Se_2$ [46].

E. Thermally activated flux flow behavior and pinning potential

We conducted temperature-dependent resistivity $\rho(T)$ measurements under various fields to determine the irreversibility critical field $\mu_0 H_{irr}$, as shown in Fig. 6(a). The criterion for determining the T_c and irreversibility temperature

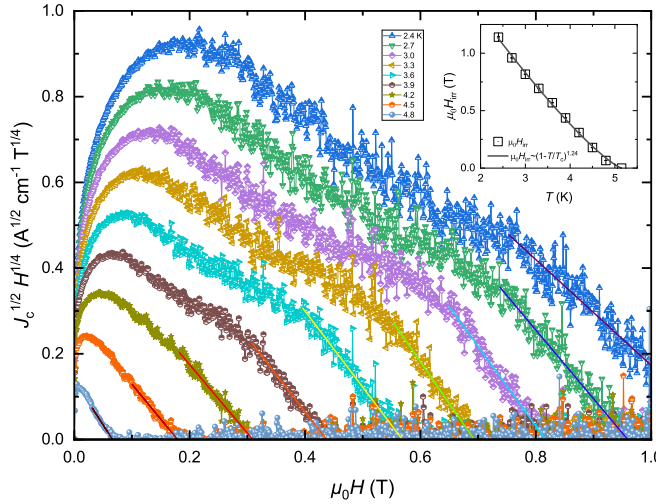

FIG. 5. Kramer plot of the $J_c(H)$ data: $J^{1/2}H^{1/4} \sim H$. Inset presents the temperature dependent $\mu_0 H_{irr}(T)$ and solid line indicates the fitting curve.

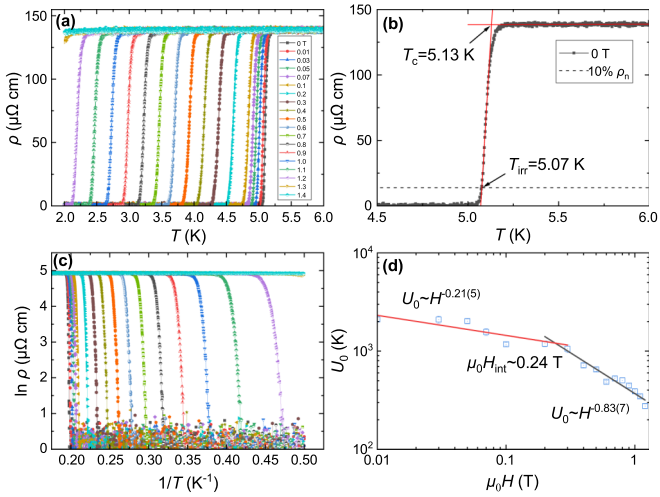

FIG. 6. (a) Temperature dependence of resistivity under various fields for $Sn_{0.55}In_{0.45}Te$. (b) Criterion determining the T_c and T_{irr}. (c) Arrhenius plot: $\ln[\rho(T,H)] \sim 1/T$. (d) Field dependence of pinning potential U_0. Solid lines are power-law fitting results.

T_{irr} is displayed in Fig. 6(b), where the $\rho(T)$ drops to 10% of the normal state resistivity [53]. The energy dissipation due to vortex motion causes the broadened resistivity at around T_c under magnetic fields, which can be described by the thermally activated flux flow (TAFF) model. In the framework of the TAFF model [54], the temperature and field-dependent resistivity $\rho(T,H)$ can be described by

$$\rho(T,H) = \rho_0 \exp\left(-\frac{U(T,H)}{T}\right), \tag{7}$$

where ρ_0 is a parameter, and $U(T,H)$ is the activation energy for the vortex bundle hopping. The Arrhenius relation

$$\ln[\rho(T,H)] = \left[\ln\rho_0 + \frac{U_0(H)}{T_c}\right] - \frac{U_0(H)}{T} \tag{8}$$

can be derived by assuming $U(T,H) = U_0(H)(1-t)$ with $t = T/T_c$ and U_0 is the pinning potential [55]. The U_0 can be extracted from the Arrhenius-plot, $\ln[\rho(T,H)] \sim 1/T$, as shown in Fig. 6(c). The obtained $U_0(H)$ is plotted in Fig. 6(d), which reaches 2.1×10^3 K at $\mu_0H = 0.01$ T. This value is comparable to the reported values of $FeS_{1-x}Se_x$ [56], $K_{0.8}Fe_{1.97}Mn_{0.03}Se_2$ ($U_0(0.25\text{ T}) = 5.1\times10^3$ K) [57], $NdO_{0.82}F_{0.18}FeAs$ ($U_0(0.2\text{ T}) = 4\times10^3$ K) [58], and $Bi_2Sr_2CaCu_2O_8$ ($U_0 = 3\times10^3$ K) [54]. Generally, the $U_0(H)$ obeys a power law $U_0 \propto H^n$ with n as a characteristic parameter for collective flux creep. The best fitting yields $n_1 = 0.21(5)$ below $\mu_0H_{int} = 0.24$ T while $n_2 = 0.83(7)$ beyond μ_0H_{int}, at which the two fitting lines intersect, as displayed in Fig. 6(d).

F. Vortex phase diagram

Figure 7 summarizes the vortex phase diagram for the $Sn_{0.55}In_{0.45}Te$ superconductor, which divides into a Meissner state, vortex solid, vortex liquid, and normal states. Hereafter, we will focus on the irreversibility field that locates fairly close to the $\mu_0H_{c2}(T)$. To calculate the GL parameter κ and London penetration depth λ, we employed a relation consid-

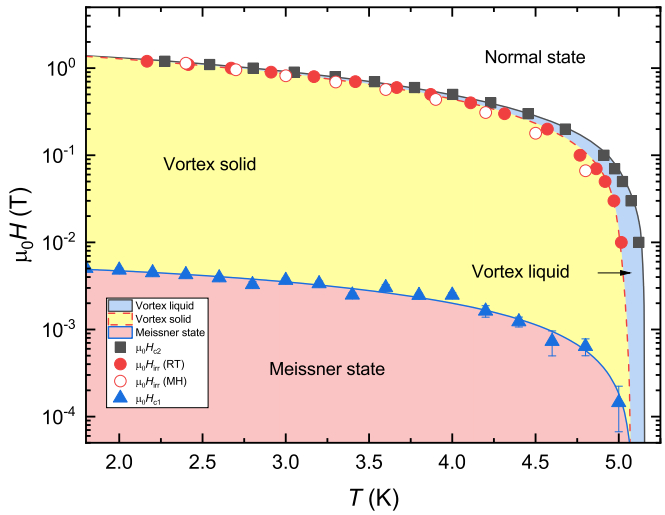

FIG. 7. Vortex phase diagram of $Sn_{0.55}In_{0.45}Te$. The solid and dashed lines are the fitting results. Meissner state: a fully diamagnetic state that does not allow the magnetic field to penetrate inside; Vortex solid: forming the vortex lattice with a well pinning by defects (pinning centers); Vortex liquid: a state that transforms from melting the vortex lattice cannot easily be pinned by defects.

ering vortex core energy as given by [59]

$$\mu_0H_{c1}(T) = \frac{\Phi_0}{4\pi\lambda^2}(\ln\kappa + 0.5), \tag{9}$$

and

$$\frac{\mu_0H_{c2}(T)}{\mu_0H_{c1}(T)} = \frac{2\kappa^2}{\ln\kappa + 0.5}. \tag{10}$$

To obtain μ_0H_{c2} at zero-temperature, we fitted the $\mu_0H_{c2}(T)$ data with the modified GL formula [60],

$$\mu_0H_{c2}(T) = \mu_0H_{c2}(0)\left(\frac{1-t^2}{1+t^2}\right)^{n_{GL}}, \tag{11}$$

where n_{GL} is a constant. The best fitting yields $\mu_0H_{c2}(0) = 1.73(1)$ T with $n_{GL} = 0.90(1)$. Combining with $H_{c1}(0) = 53(3)$ Oe, we obtained $\kappa = 25(1)$ and $\lambda(0) = 338(11)$ nm. The $\lambda(0)$ value is smaller than those of other reports, e.g., $\lambda(0) = 425$ nm and 578(2) nm for $Sn_{0.55}In_{0.45}Te$ [13,14]. Moreover, by taking the initial slope of $d[\mu_0H_{c2}(T)]/dT = -0.438(2)$ T/K and normal state resistivity $\rho_0 = 139\ \mu\Omega$ cm [61], the electronic Sommerfeld coefficient and DOS are estimated to be $\gamma = 2.47(4)$ mJ/mol K^2 and $N(E_F) = 1.05(2)$ states/eV $spin^{-1}$ f.u. The theoretical DOS value of 0.56 states/eV $spin^{-1}$ f.u. can be seen in Fig. 1(e). According to the relation $N(E_F) = (1+\lambda_{ep})N_b(E_F)$ with $N_b(E_F)$ is the band DOS, we can further obtain the electron-phonon coupling constant $\lambda_{ep} = 0.88(3)$. We note that previous reports of heat capacity studies of $Sn_{1-x}In_xTe$ by Haldolaarachchige *et al.* [62] and Kobayashi *et al.* [7] show that as increasing the In-doping content, the electronic Sommerfeld coefficient γ tends to increase. The γ value derived here is consistent with the results of the heat capacity measurements on the $Sn_{0.6}In_{0.4}Te$ [62].

A narrow critical fluctuation region width is a good ingredient for the practical use of superconducting materials.

Therefore, we evaluated its thermal fluctuations effect, which can be quantified by the Ginzburg parameter $G_i = (2\pi k_B T_c \mu_0 \lambda_0^2/\Phi_0^2 \xi)^2/2$, where μ_0 is the permeability of the vacuum, k_B is the Boltzmanns constant, and ξ is coherence length, respectively. Here, $\xi(0) = 13.8(1)$ nm is calculated using GL relation $\mu_0 H_{c2}(0) = \Phi_0/2\pi\xi^2(0)$. We obtained $G_i = 5.9(8)\times10^{-7}$ for $Sn_{0.55}In_{0.45}Te$, which is five orders of magnitude smaller than that of high-T_c cuprates (10^{-2}) [55], but comparable to that of low-T_c materials (10^{-8}) [55,63]. For more comparisons, its G_i value is smaller than other superconductors like 2H-$NbSe_2$ ($\sim10^{-4}$) [63], $CeRu_2$ ($\sim5\times10^{-4}$) [64], $Ca_3Rh_4Sn_{13}$ ($\sim3\times10^{-7}$) [48], and MgB_2 ($\sim10^{-6}$) [65]. Thus, it is expected that the small G_i value causes quite a narrow width of critical fluctuation region with Ginzburg temperature $|T_c - T| < T_c G_i = 3.0(4)\times10^{-6}$ K. This is experimentally supported by the $\mu_0 H_{irr}(T)$ at low temperature but the critical fluctuation region broadening as it approaches the T_c, as guided by the dashed line in Fig. 7. At temperatures close to the T_c, the interval is about 0.09 K between $\mu_0 H_{irr}(T)$ and $\mu_0 H_{c2}(T)$, supporting a very weak vortex fluctuation [53]. The $Sn_{0.55}In_{0.45}Te$ superconductor has a relatively narrow region between $\mu_0 H_{irr}(T)$ and $\mu_0 H_{c2}(T)$ compared to other low T_c superconductors, as reported in $FeS_{1-x}Se_x$ [56], Cu_xTaS_2 [66], $SrPd_2Ge_2$ [67] and thin film TiO [68]. Therefore, $Sn_{0.55}In_{0.45}Te$ is a promising candidate for superconducting devices applications below 5 K [17–20]. Furthermore, using the $\xi(0)$ and λ_0 values extracted before, the depairing current density [55] (the maximum current that the Cooper pairs can carry before breaking up) can be further calculated by $J_0 = \Phi_0/3\sqrt{3}\pi\mu_0\lambda^2\xi = 6.4(4)$ MA/cm^2. This results in a small ratio $J_c/J_0 \sim 4.62\times10^{-4} \ll 1$. In principle, this indicates that increasing J_c is further accessible by inducing artificial pinning centers for δT_c pinning.

Finally, we turn to discuss the potential applications as a SNSPD candidate for the $Sn_{1-x}In_xTe$ superconductors, which can be operated in liquid helium temperature. According to the photon detection model [21], several physical parameters determine the smallest photon energy ϵ that is adequate for the single photon detection regime, $\epsilon = n\Delta(T)N(E_F)k_B T_c D d \tau_{th}$, where n is a factor for the energy lost due to the generation of subgap phonons, $\Delta(T)$ is the superconducting gap, D is the electron diffusivity, d is the thin film thickness, and τ_{th} is the electron thermalization time counting the time scale of the quasiparticles multiplication. Compared to the NbN ($T_c = 9-15$ K) [69], TaN ($T_c = 8.16$ K) [70], NbSi ($T_c = 2$ K) [71], α-W_xSi_{1-x} ($T_c \leqslant 5$ K) [72] superconductors for SNSPD applications, the availability of high-quality superconducting thin films with a broad tunable T_c value below 4.2 K, uniformity as indicated by the sharp superconducting transition, higher upper critical field in the two-dimensional limit and large normal state resistivity provide practical ingredients for developing a single-photon detector in wide wavelength range for $Sn_{1-x}In_xTe$ materials [20]. On one hand, in the dirty and local limit [69], the electron diffusivity is given by $D = 1.097(-d\mu_0 H_{c2}/dT)^{-1}$ with D and $-(d\mu_0 H_{c2})/dT$ in the units of cm^2 s^{-1} and T K^{-1}. For the bulk $Sn_{0.55}In_{0.45}Te$ crystal, the D is calculated to be 2.51(1) cm^2 s^{-1}. However, as a rough estimation, the D decreases to 1.2(1) cm^2 s^{-1} and 0.17(5) cm^2 s^{-1} for out-of-plane and in-plane configuration in a 25 nm thick $Sn_{0.58}In_{0.42}Te$ thin film [20], which are comparable to that of typical NbN material ($D \sim 0.5-0.7$ cm^2 s^{-1}) [69,73]. As a SNSPD candidate, the dimension-reduction provides a practical route to access smaller D to extend the cut-off wavelength for $Sn_{1-x}In_xTe$ superconductors [21,22]. On the other hand, the quantum yield is given by $K = (1/n)(h\nu/\Delta)$ with ν is photon frequency [21]. It indicates that the lower Δ would yield a higher K ratio and thus more Cooper pairs are to be broken per photon absorption, resulting in a higher quantum efficiency. Considering the small gap ratio determined here and the other reported for the $Sn_{0.55}In_{0.45}Te$ superconductor [13], this provides a beneficial ingredient for it being as a SNSPD candidate in thin film form.

IV. CONCLUSIONS

In summary, we investigated the critical current density and vortex pinning dynamics in the superconductor $Sn_{0.55}In_{0.45}Te$. Our $H_{c1}(T)$ data supports that it has a weakly anisotropic single gap. The $J_c(T)$ curves show a nonuniversal power-law behavior with increasing field, which is ascribed to the coexistence of δT_c pinning and δl pinning regimes with field and temperature dependence. The high $J_c(0)$ and $U_0(H)$ values and very weak vortex fluctuation were demonstrated from the magnetization and electrical transport measurements. We show that the $Sn_{0.55}In_{0.45}Te$ superconductor has its potential applications in superconducting electronics like single-photon detectors in its thin film form.

ACKNOWLEDGMENTS

This work is supported by the National Natural Science Foundation of China (Grants No. 11804011, No. 11974112, No. U1930401, No. 51527801, and No. 12074153). Y.F. is sponsored by Shanghai Sailing Program No. 20YF1455100. Y.Q. is supported by the National Key R&D Program of China (Grant No. 2018YFA0704300). The authors are grateful for the support from the Analytical Instrumentation Center (No. SPST-AIC10112914), SPST, ShanghaiTech University.

[1] L. M. Rogers, J. Phys. D **1**, 845 (1968).
[2] T. H. Hsieh, H. Lin, J. Liu, W. Duan, A. Bansil, and L. Fu, Nat. Commun. **3**, 982 (2012).
[3] Y. Tanaka, Z. Ren, T. Sato, K. Nakayama, S. Souma, T. Takahashi, K. Segawa, and Y. Ando, Nat. Phys. **8**, 800 (2012).
[4] M. Zhang, X. Tang, N. Li, G. Wang, G. Wang, A. Liu, X. Lu, and X. Zhou, Appl. Phys. Lett. **116**, 173902 (2020).
[5] N. V. Morozova, I. V. Korobeynikov, and S. V. Ovsyannikov, Appl. Phys. Lett. **118**, 103903 (2021).
[6] R. D. Zhong, J. A. Schneeloch, X. Y. Shi, Z. J. Xu, C. Zhang, J. M. Tranquada, Q. Li, and G. D. Gu, Phys. Rev. B **88**, 020505(R) (2013).
[7] K. Kobayashi, Y. Ai, H. O. Jeschke, and J. Akimitsu, Phys. Rev. B **97**, 104511 (2018).

[8] J. K. Hulm, C. K. Jones, D. W. Deis, H. A. Fairbank, and P. A. Lawless, Phys. Rev. **169**, 388 (1968).

[9] T. M. Schmidt and G. P. Srivastava, Phys. Status Solidi RRL **14**, 2000362 (2020).

[10] T. Sato, Y. Tanaka, K. Nakayama, S. Souma, T. Takahashi, S. Sasaki, Z. Ren, A. A. Taskin, K. Segawa, and Y. Ando, Phys. Rev. Lett. **110**, 206804 (2013).

[11] S. Sasaki, Z. Ren, A. A. Taskin, K. Segawa, L. Fu, and Y. Ando, Phys. Rev. Lett. **109**, 217004 (2012).

[12] S. Maeda, R. Hirose, K. Matano, M. Novak, Y. Ando, and G.-Q. Zheng, Phys. Rev. B **96**, 104502 (2017).

[13] M. P. Smylie, H. Claus, W.-K. Kwok, E. R. Louden, M. R. Eskildsen, A. S. Sefat, R. D. Zhong, J. Schneeloch, G. D. Gu, E. Bokari *et al.*, Phys. Rev. B **97**, 024511 (2018).

[14] M. Saghir, J. A. T. Barker, G. Balakrishnan, A. D. Hillier, and M. R. Lees, Phys. Rev. B **90**, 064508 (2014).

[15] L. P. He, Z. Zhang, J. Pan, X. C. Hong, S. Y. Zhou, and S. Y. Li, Phys. Rev. B **88**, 014523 (2013).

[16] T. Nomoto, M. Kawamura, T. Koretsune, R. Arita, T. Machida, T. Hanaguri, M. Kriener, Y. Taguchi, and Y. Tokura, Phys. Rev. B **101**, 014505 (2020).

[17] W. Si, C. Zhang, L. Wu, T. Ozaki, G. Gu, and Q. Li, Appl. Phys. Lett. **107**, 092601 (2015).

[18] A. Bliesener, J. Feng, A. A. Taskin, and Y. Ando, Phys. Rev. Materials **3**, 101201(R) (2019).

[19] S. Fragkos, R. Sant, C. Alvarez, E. Golias, J. Marquez-Velasco, P. Tsipas, D. Tsoutsou, S. Aminalragia-Giamini, E. Xenogiannopoulou, H. Okuno, G. Renaud, O. Rader, and A. Dimoulas, Phys. Rev. Materials **3**, 104201 (2019).

[20] M. Masuko, R. Yoshimi, A. Tsukazaki, M. Kawamura, K. S. Takahashi, M. Kawasaki, and Y. Tokura, Phys. Rev. Materials **4**, 091202(R) (2020).

[21] A. D. Semenov, G. N. Golâtsman, and A. A. Korneev, Physica C **351**, 349 (2001).

[22] A. Engel, A. Semenov, H. W. Hübers, K. Il'in, and M. Siegel, J. Mod. Opt. **51**, 1459 (2004).

[23] C. J. van der Beek, M. Konczykowski, A. Abalâoshev, I. Abalâosheva, P. Gierlowski, S. J. Lewandowski, M. V. Indenbom, and S. Barbanera, Phys. Rev. B **66**, 024523 (2002).

[24] See Supplemental Material at http://link.aps.org/supplemental/10.1103/PhysRevB.106.054506 for the structural parameters information, ultra-low temperature electrical transports, and Hall effect results.

[25] A. C. L. Dreele and R. B. Von, General Structure Analysis System (GSAS), Los Alamos National Laboratory Report LAUR 86-748 (2004).

[26] B. Toby, J. Appl. Cryst. **34**, 210 (2001).

[27] P. Hohenberg and W. Kohn, Phys. Rev. **136**, B864 (1964).

[28] W. Kohn and L. J. Sham, Phys. Rev. **140**, A1133 (1965).

[29] P. E. Blochl, Phys. Rev. B **50**, 17953 (1994).

[30] G. Kresse and D. Joubert, Phys. Rev. B **59**, 1758 (1999).

[31] G. Kresse and J. Furthmüller, Phys. Rev. B **54**, 11169 (1996).

[32] G. Kresse and J. Furthmüller, Comput. Mater. Sci. **6**, 15 (1996).

[33] T. M. Schmidt and G. P. Srivastava, Comput. Mater. Sci. **182**, 109777 (2020).

[34] M. Kriener, M. Kamitani, T. Koretsune, R. Arita, Y. Taguchi, and Y. Tokura, Phys. Rev. Materials **2**, 044802 (2018).

[35] K. R. Joshi, N. M. Nusran, M. A. Tanatar, K. Cho, W. R. Meier, S. L. Budâko, P. C. Canfield, and R. Prozorov, Phys. Rev. Appl. **11**, 014035 (2019).

[36] J. Bardeen, L. N. Cooper, and J. R. Schrieffer, Phys. Rev. **108**, 1175 (1957).

[37] J. A. T. Barker, B. D. Breen, R. Hanson, A. D. Hillier, M. R. Lees, G. Balakrishnan, D. M. Paul, and R. P. Singh, Phys. Rev. B **98**, 104506 (2018).

[38] C. Ren, Z.-S. Wang, H.-Q. Luo, H. Yang, L. Shan, and H.-H. Wen, Phys. Rev. Lett. **101**, 257006 (2008).

[39] M. Kriener, K. Segawa, Z. Ren, S. Sasaki, and Y. Ando, Phys. Rev. Lett. **106**, 127004 (2011).

[40] A. Carrington and F. Manzano, Physica C **385**, 205 (2003).

[41] H. Padamsee, J. E. Neighbor, and C. A. Shiffman, J. Low Temp. Phys. **12**, 387 (1973).

[42] D. C. Johnston, Supercond. Sci. Technol. **26**, 115011 (2013).

[43] E. M. Gyorgy, R. B. van Dover, K. A. Jackson, L. F. Schneemeyer, and J. V. Waszczak, Appl. Phys. Lett. **55**, 283 (1989).

[44] A. Wang, L. Wu, V. N. Ivanovski, J. B. Warren, J. Tian, Y. Zhu, and C. Petrovic, Phys. Rev. B **94**, 094506 (2016).

[45] H. Lei, R. Hu, and C. Petrovic, Phys. Rev. B **84**, 014520 (2011).

[46] M. Li, L. Chen, W.-L. You, J. Ge, and J. Zhang, Appl. Phys. Lett. **105**, 192602 (2014).

[47] A. Duarte, E. Fernandez Righi, C. A. Bolle, F. de la Cruz, P. L. Gammel, C. S. Oglesby, E. Bucher, B. Batlogg, and D. J. Bishop, Phys. Rev. B **53**, 11336 (1996).

[48] S. Sarkar, D. Pal, S. S. Banerjee, S. Ramakrishnan, A. K. Grover, C. V. Tomy, G. Ravikumar, P. K. Mishra, V. C. Sahni, G. Balakrishnan *et al.*, Phys. Rev. B **61**, 12394 (2000).

[49] M. T. Li, Y. F. Fang, Z. Sun, J. C. Zhang, and C. T. Lin, J. Phys.: Condens. Matter **30**, 31LT01 (2018).

[50] A. I. Larkin and Y. N. Ovchinnikov, J. Low Temp. Phys. **34**, 409 (1979).

[51] R. Griessen, H.-H. Wen, A. J. J. van Dalen, B. Dam, J. Rector, H. G. Schnack, S. Libbrecht, E. Osquiguil, and Y. Bruynseraede, Phys. Rev. Lett. **72**, 1910 (1994).

[52] E. J. Kramer, J. Appl. Phys. **44**, 1360 (1973).

[53] J. Tao, Q. Deng, H. Yang, Z. Wang, X. Zhu, and H.-H. Wen, Phys. Rev. B **91**, 214516 (2015).

[54] T. T. M. Palstra, B. Batlogg, R. B. van Dover, L. F. Schneemeyer, and J. V. Waszczak, Phys. Rev. B **41**, 6621 (1990).

[55] G. Blatter, M. V. Feigel'man, V. B. Geshkenbein, A. I. Larkin, and V. M. Vinokur, Rev. Mod. Phys. **66**, 1125 (1994).

[56] A. Wang and C. Petrovic, Appl. Phys. Lett. **110**, 232601 (2017).

[57] M. T. Li, L. Chen, Z. J. Feng, D. M. Deng, B. J. Kang, S. X. Cao, C. T. Lin, and J. C. Zhang, Physica C **506**, 40 (2014).

[58] J. Jaroszynski, F. Hunte, L. Balicas, Youn-jung Jo, I. Raičević, A. Gurevich, D. C. Larbalestier, F. F. Balakirev, L. Fang, P. Cheng *et al.*, Phys. Rev. B **78**, 174523 (2008).

[59] C.-R. Hu, Phys. Rev. B **6**, 1756 (1972).

[60] M. Li, K. Xu, M. Xu, Y. Fang, Z. Yan, N. Li, Z. Yu, J. Zhang, C. Kenney-Benson, X. Wang, and L. Wang, Phys. Rev. B **100**, 224521 (2019).

[61] P. H. Kes and C. C. Tsuei, Phys. Rev. B **28**, 5126 (1983).

[62] N. Haldolaarachchige, Q. Gibson, W. Xie, M. B. Nielsen, S. Kushwaha, and R. J. Cava, Phys. Rev. B **93**, 024520 (2016).

[63] M. J. Higgins and S. Bhattacharya, Physica C **257**, 232 (1996).

[64] S. S. Banerjee, N. G. Patil, S. Saha, S. Ramakrishnan, A. K. Grover, S. Bhattacharya, G. Ravikumar, P. K. Mishra, T. V. Chandrasekhar Rao, V. C. Sahni *et al.*, Phys. Rev. B **58**, 995 (1998).

[65] T. Klein, R. Marlaud, C. Marcenat, H. Cercellier, M. Konczykowski, C. J. van der Beek, V. Mosser, H. S. Lee, and S. I. Lee, Phys. Rev. Lett. **105**, 047001 (2010).

[66] X. D. Zhu, J. C. Lu, Y. P. Sun, L. Pi, Z. Qu, L. S. Ling, Z. R. Yang, and Y. H. Zhang, J. Phys.: Condens. Matter **22**, 505704 (2010).

[67] N. H. Sung, Y. J. Jo, and B. K. Cho, Supercond. Sci. Technol. **25**, 075002 (2012).

[68] X. Liu, C. Zhang, F. X. Hao, T. Y. Wang, Y. J. Fan, Y. W. Yin, and X. G. Li, Phys. Rev. B **96**, 104505 (2017).

[69] A. Semenov, B. Günther, U. Böttger, H.-W. Hübers, H. Bartolf, A. Engel, A. Schilling, K. Ilin, M. Siegel, R. Schneider, D. Gerthsen, and N. A. Gippius, Phys. Rev. B **80**, 054510 (2009).

[70] A. Engel, A. Aeschbacher, K. Inderbitzin, A. Schilling, K. Ilâin, M. Hofherr, M. Siegel, A. Semenov, and H.-W. Hübers, Appl. Phys. Lett. **100**, 062601 (2012).

[71] S. N. Dorenbos, P. Forn-Díaz, T. Fuse, A. H. Verbruggen, T. Zijlstra, T. M. Klapwijk, and V. Zwiller, Appl. Phys. Lett. **98**, 251102 (2011).

[72] B. Baek, A. E. Lita, V. Verma, and S. W. Nam, Appl. Phys. Lett. **98**, 251105 (2011).

[73] H. Bartolf, A. Engel, A. Schilling, K. Il'in, M. Siegel, H.-W. Hübers, and A. Semenov, Phys. Rev. B **81**, 024502 (2010).